

Research Article

Detecting Turbulent Patterns in Particulate Pipe Flow by Streak Angle Visualization

Rishav Raj¹, Abhiram Thiruthummal¹, Alban Pothérat¹

1. Centre of Fluids and Complex Systems, Coventry University, United Kingdom

Detecting the transition from laminar to turbulent flow in particulate pipe systems remains a complex issue in fluid dynamics, often requiring sophisticated and costly experimental apparatus. This research presents an innovative streak visualization method designed to offer a simple and robust approach to identify transitional turbulent patterns in particulate pipe flows with neutrally buoyant particles. The technique employs a laser arrangement and a low-cost camera setup to capture particle-generated streaks within the fluid, enabling real-time observation of flow patterns. Validation of the proposed method was conducted through comparison with established techniques like Particle Image Velocimetry (PIV) and pressure drop measurements, confirming its accuracy and reliability. Experiments demonstrate the streak visualization method's capacity to differentiate between laminar, transitional, and turbulent flow regimes by analyzing the standard deviation of streak angles. The method is especially efficient at low particle concentration, ie precisely where other more established methods become less effective. Furthermore, this technique enables us to identify a critical Reynolds number using Kullback-Leibler divergence built on the statistical distribution of streak angles, which is consistent with previous studies. Because of it is effective at low concentrations and robust, this streak visualization technique opens new perspectives for the characterization of particulate pipe flows not only in the confines of the laboratory, but also in less controlled industrial multi-phase flows where determining the laminar or turbulent nature of the flow is a prerequisite for flowmeter calibration.

Corresponding author: Alban Pothérat, alban.potherat@coventry.ac.uk

1. Introduction

We introduce a particle streak-based visualization technique that is simple, cost-effective, and accurate for studying turbulence patterns and flow transitions in particulate pipe flows. The idea is to use minimal instrumentation detecting particles only to circumvent the need for separation between particles and fluid phase and offer a simple, robust method that is easy to implement in a wide variety of environments. Hence,

This method provides an accessible solution for research in engineering applications such as industrial pipelines, biological systems, and environmental processes^{[1][2][3][4]}. By analyzing particle streak angles, which reflect trajectory behavior^{[5][6]}, we use statistical tools to characterize flow states and detect turbulence with minimal disruption.

Classical single phase pipe flows dynamics exhibit subcritical transitions, where turbulence arises abruptly from finite-amplitude perturbations^{[7][8]}. While infinitesimal disturbances decay due to stability at all Reynolds numbers, finite amplitude perturbations of sufficient amplitude trigger turbulence through nonlinear mechanisms. This mechanism allows laminar and turbulent states to coexist^{[9][10]} so the transition to turbulence involves localized turbulent structures such as "puffs" and "slugs," which propagate through the pipe^{[11][12][13]}. Puffs remain confined in transitional regimes, while slugs expand and lead to fully developed turbulence at higher Reynolds numbers^{[14][15][16]}.

Technique	Measured Parameters (Two-Phase Flow)	Limitations
Dye Injection	Qualitative visualization of flow patterns and mixing regions.	No velocity quantification; ineffective in uniform-density flows.
Schlieren Imaging	Visualizes density gradients and large-scale flow structures.	Ineffective in flows without significant refractive index or density variations; qualitative only.
Hot-Wire Anemometry	Fluid Velocity using temperature fluctuations	Intrusive; unsuitable for particle-laden flows; cannot differentiate between particle and fluid velocities.
Particle Image Velocimetry (PIV)	Velocity fields of fluid phase using seeded particles.	High cost; computationally intensive; limited spatial coverage; particles must follow flow accurately.
Laser Doppler Velocimetry (LDV)	Point-wise velocity measurements of fluid phase.	Limited to single points; requires precise alignment; costly; unsuitable for dense particle suspensions.
Planar Laser-Induced Fluorescence (PLIF)	Concentration and scalar fields such as density and temperature.	Ineffective for direct velocity data; fluorescence quenching; expensive and calibration-intensive.
Ultrasound Image Velocimetry (UIV)	Velocity distribution of fluid phase in opaque flows.	Limited spatial resolution; calibration difficulties in non-homogeneous particle-fluid systems.
Magnetic Resonance Velocimetry (MRV)	3D velocity profiles of fluid phase; non-invasive.	Very slow; high cost; unsuitable for transient phenomena or rapid flow transitions.

Table 1. Comparison of Flow Visualization Techniques Their Limitations in Particulate Pipe Flow Systems

This classical problem of the laminar-turbulent transition in single-phase flows is critical for predicting fluid behavior, with Reynolds number as a key factor^{[17][18]}. Yet, many applications involve the presence of particles which may alter this scenario. Indeed, introducing even neutrally buoyant particles add complexity by modifying flow stability, altering thresholds for transition, and influencing the behavior of turbulent structures^{[19][20]}. At low concentration, neutrally buoyant particles tend to migrate to specific radial locations^{[21][22]}, under the effect of the lift force incurred by shear-induced rotation^{[23][24][25][26][27][28]}. This so-called *Segré-Silberberg* effect may even cause the base parabolic Poiseuille velocity profile to become linearly unstable at Reynolds numbers as low as 400^[29], but the subsequent nonlinear development of this instability is still unclear. In practice, these effects are important for applications ranging from pipelines to

environmental systems, where particle–fluid interactions play a significant role, and where knowledge of the flow state is a key requirement to calibrate flowmeters^{[30][31]}.

Traditional techniques for studying the stability of particulate pipe flow experimentally face significant limitations. Dye injection and schlieren imaging offer qualitative observations but lack quantitative velocity data and are ineffective for detecting fine-scale features, such as the Segre–Silberg effect^{[32][33][34][35][36]}. Hot-wire anemometry provides high temporal resolution but is unsuitable for particle-laden flows due to contamination risks and the inability to differentiate particle and fluid velocities^{[37][38]}. Its intrusive nature also disturbs the flow, limiting its effectiveness for sensitive transitional phenomena where finite amplitude perturbations need to be controlled^[39].

Modern techniques such as Particle Image Velocimetry (PIV) and Laser Doppler Velocimetry (LDV) are widely used for quantitative measurements. PIV, a planar optical technique, offers high-resolution velocity fields by analyzing the motion of seeded particles within the flow^{[40][41]}. However, it requires costly and complex setups involving high-power lasers, relatively high-speed cameras, and synchronization systems, which limit its applicability outside dedicated research laboratories^[42]. Additionally, the data processing is computationally demanding, and the system is sensitive to misalignments and calibration errors. LDV provides point-wise velocity measurements with high temporal resolution but is limited to single-point data acquisition, making it unsuitable for analyzing large-scale or spatially distributed flow features^{[43][44]}. Like PIV, LDV relies on high-power lasers and requires meticulous optical alignment, further complicating its use outside the lab^{[45][46]}.

Advanced techniques like Planar Laser-Induced Fluorescence (PLIF), Ultrasound Image Velocimetry (UIV), and Magnetic Resonance Velocimetry (MRV) are widely employed to study particle-laden flows, each with specific advantages and limitations. PLIF measures scalar fields such as concentration or temperature using laser-induced fluorescence but is unsuitable for direct velocity measurements and faces challenges like fluorescence quenching, complex calibration, and high operational costs^{[47][48]}. UIV tracks acoustic scatterers using ultrasound waves, making it particularly suitable for optically opaque or dense particle-laden systems, though it is limited by spatial resolution and calibration difficulties in non-homogeneous flows^{[49][50]}. This technique however fails for diluted particles concentrations, especially where localisation may leave large regions of the flow free of particles. MRV offers 3D velocity measurements without optical access, making it ideal for non-transparent systems, but it is hindered by high costs and long acquisition times^{[51][52]}. While these methods are effective, their reliance on expensive and complex setups restricts their applicability. Furthermore, while the extensive data they deliver makes them suitable for detailed mapping of the flow, the limited purpose of detecting flow patterns may be fulfilled with much less extensive

datasets delivered by simpler setups. Additionally, existing methods often struggle to capture transient structures like puffs and slugs over the full pipe length due to high costs, accessibility issues, or safety constraints. As shown in Table 1, various flow visualization techniques have distinct limitations in particulate pipe flow systems. These challenges stress the need for scalable, versatile solutions for both research and industrial applications.

Most existing methods are impeded by the coexistence of the solid phase (particles) and the liquid phase. To circumvent these issues, we propose to use a less sensitive setup that only detects particles, and that is not affected by the fluid phase. The main idea is that where turbulence exists in the fluid phase, neutrally-buoyant particles should follow erratic trajectories, whereas in laminar regions their trajectories should be close to straight lines aligned with the pipe axis. The challenges here are to introduce a meaningful way to mathematically distinguish these two types of trajectories, and also to verify that they reliably map to turbulent and laminar states of the fluid phase, respectively. For these purposes, the streak-based visualization technique we present in this paper combines simplicity with robust statistical tools. Using the standard deviation of particle streak angles, we classify flow regimes and turbulent features, while the Kullback-Leibler divergence provides a novel method for determining the critical Reynolds number, effectively capturing the laminar-to-turbulent transition. This approach is particularly suited for low-particle-concentration flows and transparent fluids, where traditional methods are less effective. By addressing these current limitations and offering a cost-effective alternative, this method offers new perspectives to study transitional particulate flows at low concentration. Its principle may also be implemented to develop instrumentation capable of rapidly identifying turbulent pattern in constrained industrial environment.

The paper is laid out as follows: we first describe the experimental setup (section 2, the streak-visualisation system and associated data processing technique (section 4). We then validate the identification of flow patterns against classical PIV, PTV and pressure measurement techniques. Finally, we show how a simple measure of the standard deviation of the angle of particle trajectories enables us to detect turbulence flow patterns. We also show that more refined properties of the statistical distribution of these angles offer a way to define a critical Reynolds for the transition to turbulence consistent with previous studies (section 5).

2. Experimental Setup

The experimental setup is an upgrade of the setup described in detail in^[53]. It consists of several subsystems, all represented in Figure 1. The pipe and hydraulic elements form the main component, through which the fluid and the particles travel. The glass pipe assembly comprises 10 cylindrical borosilicate glass tubes, each 1.2 *m* long, with a bell mouth inlet and an additional 25 *cm* glass section at the outlet. The pipe

sections are of lengths $1.2\text{ m} \pm 10\text{ }\mu\text{m}$ -to- $30\text{ }\mu\text{m}$, an inner bore diameter of $D = 20\text{ mm} \pm 0.01\text{ mm}$, and a wall thickness of $3.1\text{ mm} \pm 0.03\text{ mm}$ and are manufactured to high precision to minimize disturbances caused by geometric irregularities. This setup is designed to experimentally study the effects of solid, neutrally buoyant, spherical particles on the transition to turbulence in dilute particle-laden pipe flows.

The first upgrade to the original system is a change of working fluid, tracers, and particles that makes the rig now operable with water with the addition of a small amount of glycerol used to precisely match fluid and particle densities. This adjustment results in a fluid density (ρ_f) of 1000 kg m^{-3} , composed of 98.4% water and 1.6% glycerol. The dynamic viscosity of the final solution is approximately $\mu = 1.13 \times 10^{-3}\text{ Pa s}$.

This mixture is easier to handle than the aqueous solution of Sodium Polytungstate that was initially chosen to match the density (2500 kg/m^3) of glass particles used to seed it. This change is made possible by the availability of opaque polyethylene particles of density close to that of water. Two types of particles are required to study particulate flows: the first ones are tiny silver-coated hollow glass particles (in the size range of $10\text{ }\mu\text{m}$) that follow the flow almost instantaneously and are used for Particle Image Velocimetry. For the remainder of this paper, these particles are referred to as *tracers*. To act like tracers, the particles' response time needs to be much smaller than the time scale of the flow, or equivalently, their Stokes number $St = \rho d_p^2 U / (18\mu D)$ has to be much smaller than unity.

In our experiments, the tracers' Stokes number is within the range $[7 \times 10^{-6}, 2 \times 10^{-4}]$, and so fulfills this criterion.

The second type of particles, on the other hand, are much larger particles, with St close to unity, alter the dynamics of the fluid phase, and are used to study the particulate flow dynamics that result from the interaction between those two phases. Two ranges of diameter particles are utilized: the first type has diameters d_p ranging from $425\text{ }\mu\text{m}$ -to- $500\text{ }\mu\text{m}$, while the second type ranges from $212\text{ }\mu\text{m}$ -to- $250\text{ }\mu\text{m}$. The particle-to-pipe diameter ratios are respectively between $[0.0212, 0.025]$ and $[0.0106, 0.0125]$. The particle concentration during experiments is kept at $C = 1.2\text{ kg m}^{-3}$, corresponding to a volume fraction of $\Phi = 1.2 \times 10^{-3}$ in all cases.

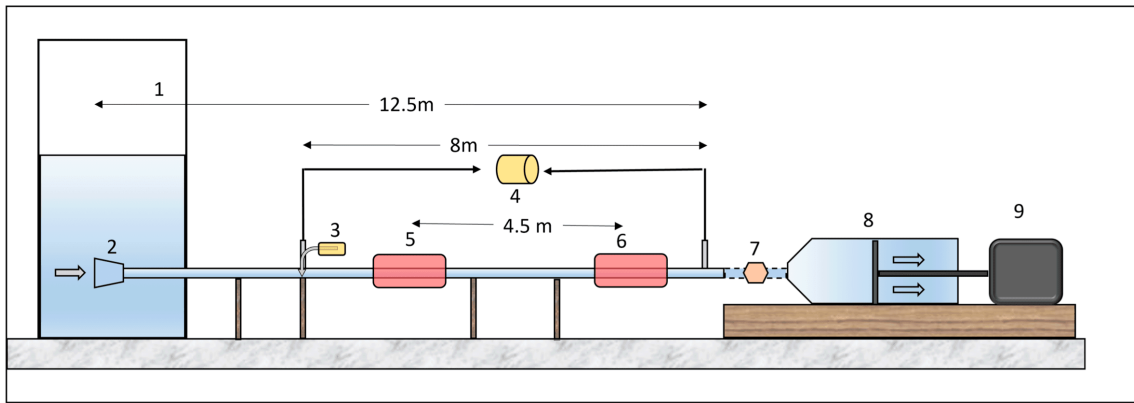


Figure 1. A 2-D schematic diagram of the rig. (1) Fluid Reservoir, (2) Bell-mouth inlet, (3) Perturbation system, (4) Differential pressure meter, (5) 1st visualization system, (6) 2nd visualization system, (7) Mass flow meter, (8) Piston-cylinder arrangement, (9) Motor

Upstream of the pipe, the system is fed by a reservoir where the fluid is stored. A bell mouth inlet placed inside this reservoir allows a smooth entry of the fluid into the pipe. The other end of the pipe is connected to a piston-cylinder arrangement driven by a motor. The fluid from the reservoir is pulled through the pipe when this motor pulls the piston, thus creating a pressure difference and driving the flow.

The second subsystem is aimed at introducing precisely controlled velocity perturbations perpendicular to the mean flow. This perturbation subsystem is made of a syringe attached to a stepper motor, connected to the main pipe 4.5 m downstream of the inlet. The diameter of the perturbation injection inlet is $d_{pert} = 2.2 \text{ mm}$. The stepper motor is controlled by an Arduino that sets the volume and flow rate of the injected perturbation. The effect of the introduced perturbation on the fluid-particle system is visualized at two downstream locations by two different measurement systems.

The 1st visualization system consists of a powerful 1 W laser and a high-speed camera used for simultaneous Particle Tracking Velocimetry (PTV) and Particle Image Velocimetry (PIV). The purpose of this system is to independently and simultaneously track large particles and map flow velocities by PIV in a vertical plane aligned with the pipe axis, lit by the laser. The visualization section is located 400 pipe diameters (8 m) from the center of the section to the pipe inlet. The details of this technique can be found in Ref. [53].

The newly developed streak visualization system, positioned as the 2nd visualization setup, is centered 225 pipe diameters (4.5 m) downstream from the center of the 1st visualization system, following the PTV/PIV setup.

Figure 2 shows a 2-D lateral view and a picture of this streak visualization setup placed in the rig. The visualization system employs a 50 *mW* laser and a Flea camera (Blackfly-FLIR). The camera's resolution is set to 1536 x 2048 pixels, and it is equipped with a 35 *mm* focal length lens. The sensor size is approximately $4.8 \times 10^{-3} \text{m} \times 3.6 \times 10^{-3} \text{m}$. The gain is adjusted to prevent excessive brightness. The opaque particles, introduced into the fluid under examination, reflect the laser light sheet. The camera is oriented perpendicular to the laser sheet and captures images with adjusted exposure time varying from 15 *ms*-to-50 *ms*, for the range of Reynolds number considered in this paper $Re = \frac{UD}{\nu} \in [1120, 2980]$. Here U , used to calculate the Reynolds number, is the average velocity of the fluid across the entire cross-section of the pipe, calculated by dividing the volumetric flow rate by the cross-sectional area.

This camera setting is chosen to ensure that the captured images depict the particles as distinct streaks of light, thus providing a visual representation of the angles subtended by the path of the particles, with respect to the pipe axis.



Figure 2. 2-D diagram of the lateral view of streak visualization setup (left) and picture of the actual streak visualization system (right) for streak-angle velocimetry. (a) laser, (b) laser sheet, (c) glass pipe, and (d) camera and lens.

Lastly, the test rig is also fitted with a high-speed differential pressure transducer (Omega USBH Series). It is a USB-based device and comes with its own software for direct recording in the computer. It has a range of 0 *mbar*-to-70 *mbar*, with an accuracy of $\pm 0.08\%$ and a sampling frequency of 1000 *Hz*. The differential pressure is measured across the pipe between the point of injection of the disturbance and the pipe's end

section over a distance of 8.3 *m*. An extra 20 *cm* glass section with a T-inlet is manufactured separately and connected at the end of the pipe to connect it there.

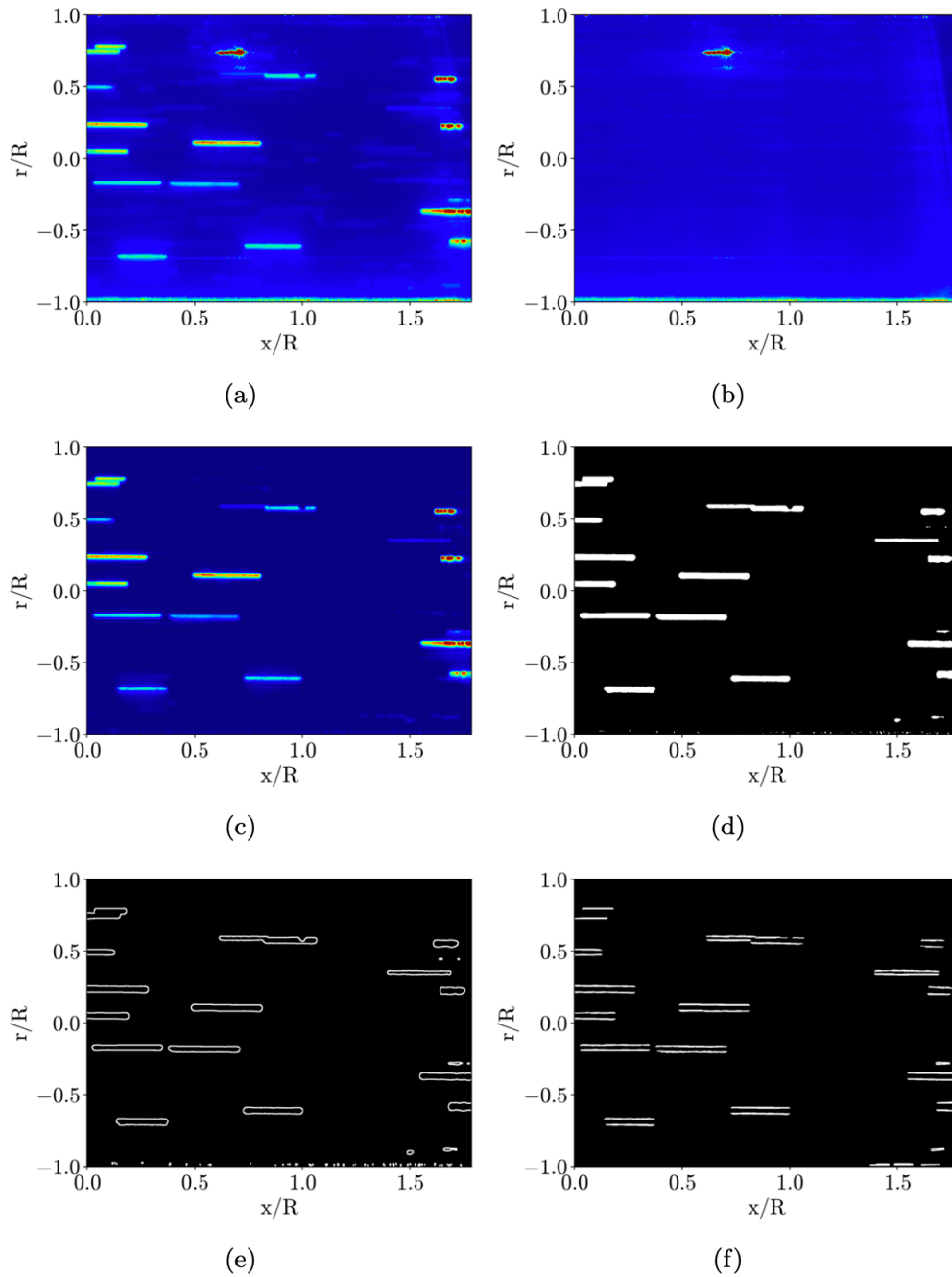


Figure 3. Successive stages of image processing for the streak-angle velocimetry. In the vertical axis, r/R means a location r from the centreline for the given pipe radius R . In the horizontal axis, x/R is the distance x from the left of the image with respect to R . (a) Raw image, (b) background frame obtained from the average of all pictures within a run, (c) image after background subtraction, (d) image after adaptive thresholding, (e) image after canny edge detection and (f) Lines detected by Hough transform (showing the two lines counted as one per actual streak).

2.1. Experimental Control Parameters

The problem is governed by the following non-dimensional numbers: As in the non-particulate pipe flow, the Reynolds number $Re = UD/\nu$ measures the ratio of inertial to viscous forces outside the laminar regime and is varied in the range [1120, 2980]. The addition of neutrally buoyant spherical particles, of density ρ and diameter d_p , introduces two additional parameters: the particle-to-fluid volume fraction (Φ), set to $\Phi = 1.2 \times 10^{-3}$, and the Stokes number $St = \rho d_p^2 U / (18\mu D)$ measuring the ratio of the particle's relaxation time under the effect of drag exerted by the fluid, $\tau_p = \rho d_p^2 / 18\nu$, to the fluid's advection time $\tau_U = D/U$. For the particles, St is in the range [0.2, 0.6]. In practice, Re , Φ , and St are controlled through the piston's velocity that imposes the mass flux, the volume of particles introduced in the fluid, and the particles' diameter respectively.

Additionally, the flow perturbation introduces a radial mass flux through the perturbation inlet controlled dimensionally through the total volume of fluid introduced V' , here set to 1ml or 0.5ml, and the time of application of the perturbation τ' , here set to $\tau' = 90$ ms. To non-dimensionally measure the perturbation for a given τ' , we introduce the perturbation Reynolds number (Re_{pert}), which is analogous to the conventional Reynolds number and is defined using the averaged fluid velocity, obtained by dividing the volumetric perturbation flow rate with its pipe cross-sectional area calculated using its inner diameter. Two distinct values, $Re_{\text{pert}} = 3200$ and $Re_{\text{pert}} = 6400$, corresponding to perturbation volumes of 0.5 ml and 1 ml respectively, are employed in this study. Table 2 provides an overview of the control parameters used in this study.

Parameter	Range / Value
Reynolds number (Re)	[1120, 2980]
Particle-to-fluid volume fraction (Φ)	1.2×10^{-3}
Particle Stokes number (St)	[0.2, 0.6]
Perturbation Reynolds number (Re_{pert})	3200, 6400

Table 2. Experimental Control Parameters

The parameters are chosen to cover a sufficiently large range of flow patterns for the purpose of their characterization by the streak-angle visualization method.

2.2. Experimental procedure

We use the following experimental procedure: To initiate the experiment, the fluid-particles-tracers mixture is circulated upstream and downstream of the pipe to ensure particle and tracer homogeneity. The flow is then gently reversed to expel air bubbles, directing them out at the reservoir side. Afterward, the system is left idle for 25 minutes to allow the fluid to reach a standstill state. The motor, controlling the piston-cylinder arrangement, is then set to a specific rotation speed to achieve the target Reynolds number Re .

Once the flow is fully developed—ensured by positioning the perturbation system 225 D downstream of the reservoir inlet^[54]—a controlled perturbation is introduced. This placement does not simply indicate that the flow has exited the acceleration phase; rather, it confirms that the flow has reached a steady, fully established state as dictated by the inlet conditions.

The first visualization system, combining Particle Tracking Velocimetry (PTV) and Particle Image Velocimetry (PIV), captures high-resolution flow images timed with the perturbation's arrival and provides us with a detailed analysis of the velocity field. Then, the second visualization system is used to perform streak visualization on flow patterns resulting from the downstream evolution of the flow within the fluid volume captured by the first system. Particle streaks are recorded to analyze downstream flow patterns and perturbation evolution.

The differential pressure transducer continuously monitors the pressure drop across the pipe during the entire run. The system is reset, the fluid re-mixed, and allowed to settle as described above between each run to ensure consistent experimental conditions.

3. Image Processing for the Streak Visualization System

The image processing for the streak visualization system is carried out using the OpenCV library in Python^[55]. The primary goal of this process is to detect the lines corresponding to the streaks visible in the image and then accurately extract the angles that these lines form with the pipe axis. This information is crucial for understanding the dynamics and flow characteristics within the pipe.

The initial step in this process involves capturing raw images from the camera during the experiment (Figure 3a). These raw images often contain various artifacts caused by the reflection of light from the surface of the pipe, which can interfere with the accurate detection of streaks. To address this issue, a background frame (Figure 3b) is constructed by averaging all the frames captured during each experimental run. The purpose of this background frame is to capture the persistent elements of the image that are not of interest, such as static reflections and uniform lighting patterns. By subtracting this background frame from

each raw image, we obtain a background-subtracted image (Figure 3c), which is significantly cleaner and free from most artifacts. This subtraction step is essential to isolate the dynamic features, i.e., the streaks, from the static background.

After obtaining a cleaner, artifact-free image, the next step is to identify the streaks within the image. This is accomplished by converting the image into a binary format, where the pixels corresponding to the streaks are assigned a value of 1 (white), and the background pixels are assigned a value of 0 (black). This binarization is typically achieved through thresholding techniques. In simple or global thresholding, a single threshold value is applied across the entire image: pixels with values above this threshold are set to 1, and those below are set to 0. However, this approach is often insufficient for our application due to the uneven lighting and varying brightness of the streaks across different regions of the image.

To address these challenges, an adaptive thresholding algorithm is employed. Unlike global thresholding, adaptive thresholding calculates the threshold for each pixel based on the pixel values in its local neighborhood. In our methodology, we use a neighborhood defined by a square window with a side length of 101 pixels centered on the pixel of interest. The threshold for each pixel is set to the mean value of the pixels within this window minus a constant C . For our experiments, we have empirically determined the optimal value of C to be 8. The images captured have an 8-bit depth, meaning each pixel can have an intensity value ranging from 0 (black) to 255 (white). The choice of the adaptive thresholding parameters, such as the neighborhood size and the constant C , is made based on careful visualization and experimentation specific to our setup, as illustrated in Figure 3d. These parameters are critical and are influenced by factors such as the bit depth, sensitivity, and resolution of the camera, as well as the illumination conditions during the experiment. In cases where the images are noisy or grainy, it is advantageous to apply Gaussian smoothing before performing adaptive thresholding. This smoothing step reduces noise and enhances the quality of the binary image, making the subsequent streak detection more accurate.

Once the binary image is obtained, the next step involves detecting the streaks as lines. A common approach for line detection is the Hough transform^{[56][57]}, which is effective in identifying lines in binary images. However, directly applying the Hough transform to our binary images can lead to multiple lines being detected for a single streak due to the non-negligible thickness of the streaks. This multiplicity would skew the analysis, as the number and angles of detected lines would incorrectly reflect the streaks' actual characteristics. To prevent this, we first apply the Canny edge detection algorithm^[58], which is designed to detect the edges of objects in an image. By detecting the edges of the streaks (Figure 3e), we can then apply the Hough transform to these edges, resulting in a more accurate representation of the streaks as lines. The Canny edge detection algorithm, as implemented in OpenCV, involves several parameters, including the minimum and maximum thresholds and the aperture size, which determines the size of the matrix used for

the derivative computation. Since our image is binary, the results are relatively insensitive to the specific threshold values, and we have selected the smallest aperture size of 3 to ensure precise edge detection.

For the line detection itself, we employ a probabilistic variant of the Hough transform^[59]. This variant significantly reduces the computational load by considering only a random subset of points in the image for line detection, with a minor trade-off in accuracy. The parameters for the OpenCV implementation of this probabilistic Hough transform are carefully chosen to balance detection accuracy and computational efficiency. Specifically, we set the distance resolution to 1 pixel, the angle resolution to 1 degree, an accumulator threshold of 30 votes, a minimum line length of 30 pixels, and a maximum line gap of 20 pixels. The term "accumulator threshold" refers to the minimum number of votes required for a line to be detected. Each vote indicates a point in the image supporting the presence of a line at a particular position and angle. Setting a threshold of 30 votes ensures that only prominent lines, with sufficient supporting points, are identified. These parameters ensure that the detected lines correspond closely to the actual streaks in the image while minimizing the detection of spurious lines due to noise or minor image imperfections.

In summary, the detection of streaks in images involves a sequence of well-defined steps: background subtraction to remove artifacts, adaptive thresholding to create a binary image, Canny edge detection to identify the edges of streaks, and the probabilistic Hough transform to detect the streaks as lines. Each step is carefully tailored to the specific needs of the experimental setup, including the characteristics of the imaging system and the environmental conditions. The empirical selection of parameters for adaptive thresholding, edge detection, and Hough transform is crucial for the robustness of the system, ensuring that the detected lines accurately represent the streaks and that the angles extracted are reliable for further analysis.

4. Flow state identification based on the fluid phase

4.1. Identification of flow pattern using PIV

We start by characterizing the flow state using traditional techniques based on the full flow field delivered by PIV measurements from the first system. Patterns are identified by analyzing centerline velocity, velocity fluctuations, and average axial velocity profiles from PIV data. In the laminar phase, the average velocity profile matches closely with the Hagen–Poiseuille profile, indicating steady flow with minimal fluctuations. The transitional flow features such as puffs are identified by analyzing characteristic velocity fluctuations. Puffs are detected as localized turbulent structures with distinct leading and trailing edges (fronts and tails). As they pass a point along the pipe, they cause transient drops in centerline velocity while the flow upstream and downstream of a puff remains laminar. In the turbulent phase, the profile is approximately aligned to

the 1/7th power-law profile, with high-frequency fluctuations and irregular spatial variations. These distinct profiles and centerline changes enable the precise identification of laminar, transitional, and turbulent flow states.

The flow patterns observed in response to $Re_{\text{pert}} = 3200$ and $Re_{\text{pert}} = 6400$ ($\phi = 1.2 \times 10^{-3}$, particle size range = 212 – 250 μm) when the fluid Reynolds number is increased, are reported in Table 3. For smaller Re , i.e. $Re = 1120$ and $Re = 1530$, the flow is laminar. However, a transition to localized turbulence takes place at at most $Re = 1980$, as puffs are detected for this value. In these cases, turbulent patches ('Puff') appear within an otherwise laminar flow, signifying the onset of turbulence within the system. For $Re \geq 2260$, the turbulent nature of flow takes over.

The state of particulate pipe flows is usually characterized using the perturbation intensity $\epsilon = (d_p/D)^{\frac{1}{2}} (\phi)^{\frac{1}{6}}$. The critical Reynolds number $Re_{s,c}$, marking the onset of turbulence, scales as $Re_c \sim \epsilon^{-1}$. This inverse relationship implies that as particle perturbations grow (via increased particle size or concentration), turbulence initiates at lower Reynolds numbers^[30]. For the parameters we consider, $\epsilon \in [0.033, 0.0515]$, and so the transition is expected to take place in the range $Re_c \in [2200, 2400]$, when our measurements capture the presence of puffs at $Re = 1980$ and transition in the region $Re_c \approx 2260$, well within the expected range. On this basis, our results are consistent with the literature^{[30][60][20]}.

Parameters: $Re_{\text{pert}} = \{3200, 6400\}$, $\phi = 1.2 \times 10^{-3}$, Particle size range = 212–250 μm						
Reynolds Number	1120	1530	1980	2260	2550	2980
Flow State (PIV)	Lam	Lam	Puff	Turb	Turb	Turb
Flow State (Streak Visualization)	Lam	Lam	Puff	Turb	Turb	Turb

Table 3. Observed flow patterns in a particulate flow using PIV and Streak Visualization (described in section 5). 'Lam' and 'Turb' correspond to laminar and turbulent flow states extending over several diameters, while 'Puff' corresponds to a small turbulent patch, typically less than a pipe diameter long inside an otherwise laminar flow.

4.2. Utilization of Pressure Drop Measurements to Characterize Particulate Pipe Flow States

Identifying flow patterns from measurements at a single observation point in the pipe suffers from uncertainty due to the evolution of the turbulence along the pipe: decaying regions of turbulence cannot be distinguished from expanding ones, so laminar and turbulent states cannot be distinguished with full certainty over long pipe ranges. The issue is alleviated by using the differential pressure meter to assess the

pressure drop between the point where the perturbation is injected into the flow and the pipe's outlet. The pressure drop is controlled by the state of the fluid phase, and so offers a way to diagnose the turbulent or laminar state of the flow that is independent of the two visualization systems and crucially, regardless of how turbulent patches may evolve when traveling between the two systems. Of course, this method still misses the dynamics of turbulent patches decaying or growing over timescales much longer than the finite length of the rig can capture.

Using the differential pressure measurements, we calculate the friction factor based on the formula provided in Eq. (1):

$$f = \frac{2D\Delta P}{\rho LU^2}, \quad (1)$$

where ΔP is the measured pressure difference. We then map the experimentally determined friction factors with the theoretical friction factors for a pure fluid in both the laminar and turbulent regimes, as given by Eqs. (2) and (3), respectively. In the laminar flow region, the friction factor follows the Hagen-Poiseuille law for a single fluid:

$$f_{\text{lam}} = \frac{64}{\text{Re}} \quad (2)$$

In contrast, in the turbulent flow region, the friction factor for a smooth pipe is described by the Kármán-Prandtl resistance equation^[61]:

$$\frac{1}{\sqrt{f}} = 1.930 \log\left(\frac{\text{Re}}{\sqrt{f}}\right) - 0.537 \quad (3)$$

On this basis, we obtain friction from Eq. (1) and compare it with those of (2) and (3) respectively. This gives an estimate of the flow state across the pipe length.

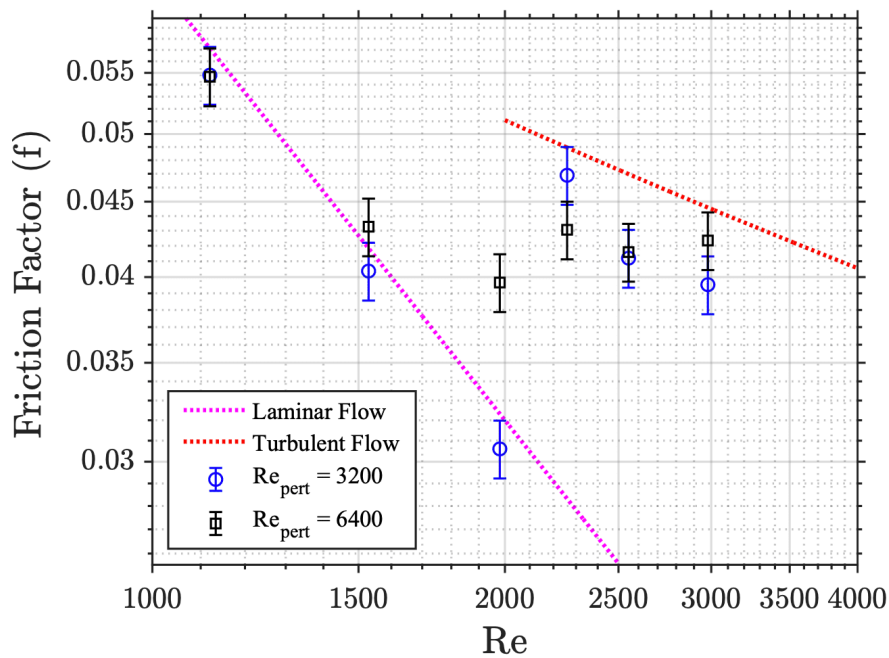
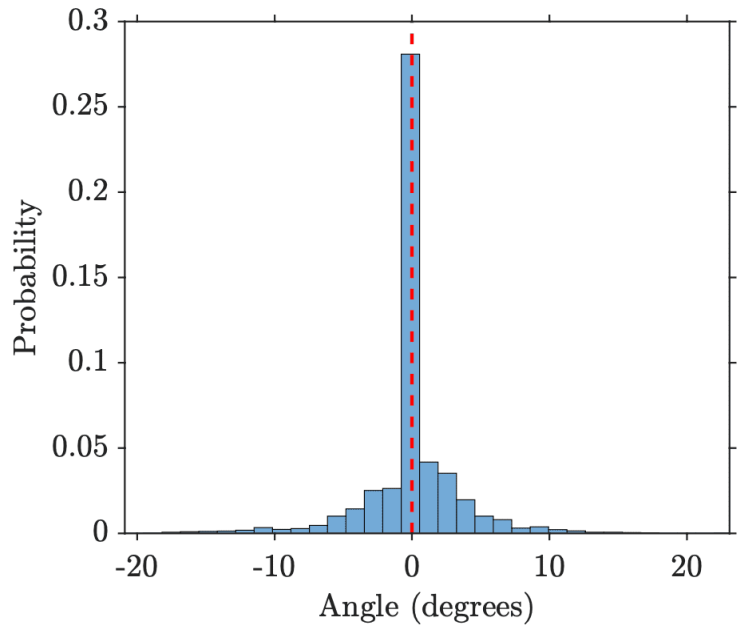


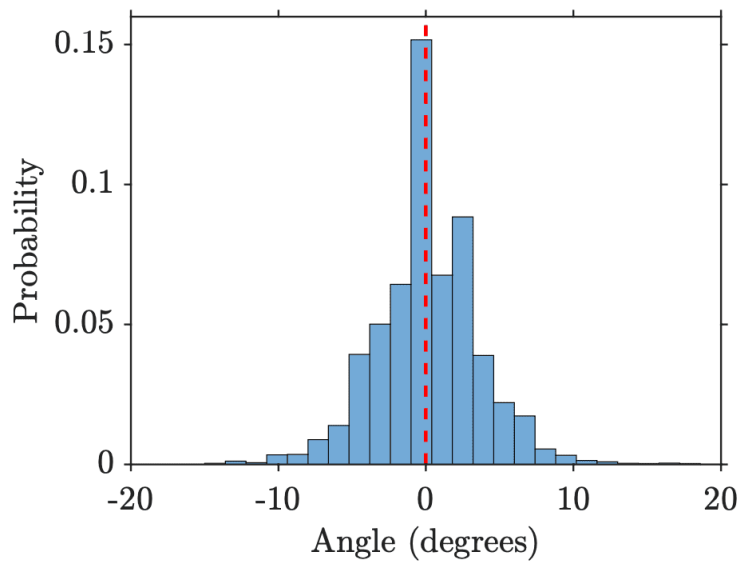
Figure 4. Friction factor vs Re based on the pressure drop readings obtained from the particulate pipe flow experiment ($\phi = 1.2 \times 10^{-3}$, particle size range = 212–250 μm) against theoretical laminar and turbulent flows.

The measured friction factors for the cases of $Re_{pert} = 3200$ and $Re_{pert} = 6400$ ($\phi = 1.2 \times 10^{-3}$, particle size range = 212 – 250 μm) are plotted against Re in Figure 4. For $Re_{pert} = 3200$, $Re = 1120$ and 1530 , the friction follows the law for a single-phase laminar flow. At $Re = 1980$, although the flow exhibits puffs detected by the Particle Image Velocimetry (PIV), see Section 3, the friction still coincides with its predicted laminar value, meaning that the puff was a localized feature and did not grow over the pipe length. However, for Reynolds numbers of 2260 and higher, the friction takes a value between the laminar law and the friction law for a fully developed turbulent single-phase flow, indicating that the flow is turbulent in part of the region between the two pressure measurement points. When the friction is close to the turbulent friction value, the the flow between the two measurement points is turbulent in most of the pipe.

Additionally, for $Re_{pert} = 6400$, the friction factor regime is similar to that obtained from $Re_{pert} = 3200$ except for $Re = 1980$, indicating that for a higher Re_{pert} the puff probably survives and grows to fully developed turbulence, and so affects the friction factor. Nonetheless, the intermediate value between the fully laminar and the fully turbulent one tells us that turbulence occupies only part of the pipe length, so the flow is still in the transitional flow regime and not fully turbulent.



(a)



(b)

Figure 5. The depicted figures illustrate the probability distribution histograms of streak angles for two distinct Reynolds number scenarios ($\phi = 1.2 \times 10^{-3}$, particle size range = 212 – 250 μm). Figure (a) represents the streak angle distribution for the case with Re 1120, while Figure (b) portrays the streak angle distribution for the scenario with Re 2980.

The results in this section show that combining PIV and pressure drop measurements both validate and complement each other. This enables us to reliably diagnose the flow state and gives us confidence in using them to validate the streak visualization method, which is the main point of this work.

5. Characterisation of the flow states using streak-visualisation

5.1. Streak visualisation

A key difference between streak visualization and the techniques used in the previous section is that it relies on the movement of the particles, not the fluid phase. Hence, assessing the laminar or turbulent state of the flow in this manner demands that the motion of the particles reflects these states in an unequivocal way. While the particles (with $St \sim 1$) do not follow the trajectories of the fluid, the main question is whether their trajectories display turbulent features (i.e. erratic, misaligned) when the fluid phase is turbulent and laminar (i.e. rectilinear and aligned in the streamwise direction when the fluid phase is laminar). Hence we first seek to characterise whether this is the case by instantaneous visualising snapshots of streaks corresponding to either flow regimes.

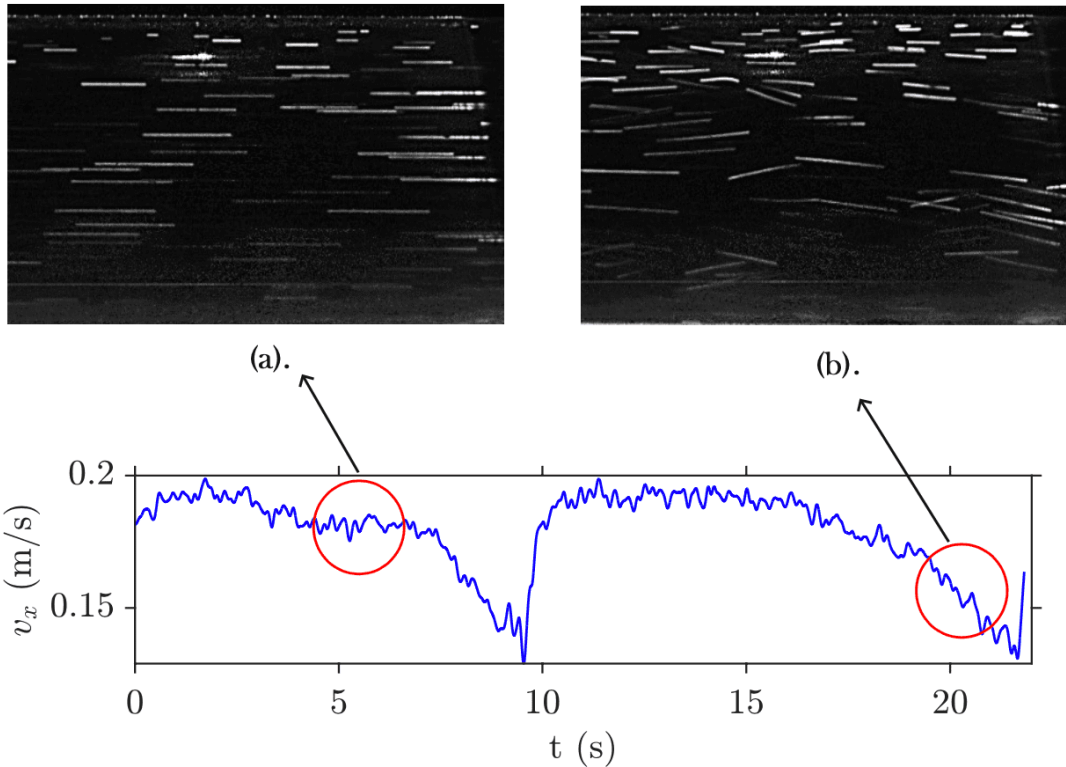


Figure 6. The blue line is the temporal centreline velocity of the fluid obtained from the PIV system at Re 1980 ($\phi = 1.2 \times 10^{-3}$, particle size range = 212 – 250 μm) showing the passing of two puffs. The two images (a and b) shown here are obtained directly from the camera of the streak visualization setup and show the streaks produced by the particles. Both images are taken at Re 1980, but (a) is the part where the flow is laminar, and (b) captures the turbulent puff.

To this end, the images (a and b), as depicted in Figure 6, are captured directly from the camera of the streak visualization setup, showcasing the streaks generated by the particles within the fluid flow. An example is shown in figure 6. Two images are shown at $Re = 1980$ ($\phi = 1.2 \times 10^{-3}$, particle size range = 212 – 250 μm). Image 6(a) corresponds to an instant where the flow is laminar, where streaks are qualitatively well aligned with the streamwise direction. Image 6(b) captures one instant during the passage of a turbulent puff and shows streaks at finite angles with the streamwise direction. These images 6 (a and b) are approximately taken at positions indicated by red circles overlaid on the centerline velocity profile obtained from the PIV setup. This positioning highlights a visible variation in streak angles between the laminar and turbulent regions of the fluid flow. Specifically, the observed change in streak angle serves as a visual indicator of the dynamics over the short exposure time of the camera, which compared to the global flow timescale is nearly instantaneous. This difference was noticeable in all examples and all instants where the flow could be clearly

identified as being laminar or turbulent. As such, streak visualization based on the particles potentially makes it possible to follow the time evolution of the state of the fluid phase. To achieve this at every instant of a series of recorded images and monitor the evolution of the flow state in time, a large number of consecutive images must be processed, so we need an quantitative criterion to identify the flow state in each streak snapshot.

5.2. Flow behavior identification based on the standard deviation of streak angles

To quantify the distribution of streak angles with respect to the centreline, we plot the binned probability distribution of angles for two typical cases. The result, illustrated in Figure 5, demonstrates a clear disparity in the angle distributions between cases for two different Re numbers ($Re = 1120$ and $Re = 2980$ ($\phi = 1.2 \times 10^{-3}$, particle size range = 212 – 250 μm)). In the histogram representation, angles cluster towards zero degrees in laminar flows, signifying a more uniform directionality of particle streaks. Conversely, in relatively turbulent flows, the angle distribution is notably wider, reflecting the chaotic nature of particle motion within the fluid. This reflects the qualitative impression obtained by observing snapshots of streaks in laminar and turbulent flow states in the previous section. Indeed, differentiating between the two cases is often easy by simply looking at the picture. There are, however, cases where transitional features are difficult to differentiate. Hence, there is a need for a more systematic approach to the detection of patterns from pictures. The simplest approach to this problem is to imitate "human recognition" in its most basic form: when assessing whether streaks are mostly horizontally aligned or more randomly distributed, we assess an average distribution and its scattering, *i.e.*, the standard deviation of the angles (the average is always expected to be close to 0 provided there is a sufficiently large number of streaks in the picture considered).

However, to quantify the orientation of the streaks with sufficient statistical convergence, we consider the distribution of streak angles over multiple frames. The mean and standard deviation of these angles are calculated over a moving window of 5 frames. Increasing the number of frames used for computing the statistics decreases the error and noise in the estimates but decreases the temporal resolution of various features of interest. Decreasing the number of frames has the opposite effect. Hence, there is a trade-off between time resolution (which is improved by a higher sampling frequency, hence by reducing the number of successive frames used for the determination of the standard deviation) and statistical convergence.

We denote the set of streak angles obtained from 5 consecutive frames as $\{\theta_{i,i_n}\}$, where i varies from 1 to 5 denotes the frame and i_n denotes the streak angles in the i^{th} frame. The standard deviation σ of these values measures the dispersion or spread of the angles around their mean value. Mathematically, the sample standard deviation σ is calculated as follows:

$$\sigma = \sqrt{\frac{\sum_{i=1}^5 \sum_{i_n} (\theta_{i,i_n} - \bar{\theta}_i)^2}{\left(\sum_{i=1}^5 \sum_{i_n} 1\right) - 1}}, \quad (4)$$

where $\bar{\theta}$ is the mean of the set of angles $\{\theta_{i,i_n}\}$ given by:

$$\bar{\theta} = \frac{\sum_{i=1}^5 \sum_{i_n} \theta_{i,i_n}}{\sum_{i=1}^5 \sum_{i_n} 1}. \quad (5)$$

A higher standard deviation σ indicates greater variability in the streak angles across the frames. When the fluid flow is laminar, the streak angles tend to align parallel to the reference axis (e.g., horizontal), resulting in a lower standard deviation. In contrast, turbulent flow leads to irregular and chaotic movement of particles, causing streaks with varying angles, resulting in a higher standard deviation.

We analyze the angles of streaks produced by particles in a fluid, focusing on their distribution characteristics under laminar and turbulent flow conditions. The angles of these streaks are indicative of the underlying flow properties, with laminar flows typically exhibiting narrower angle distributions tending towards zero degrees, while turbulent flows display broader and more spread-out distributions.

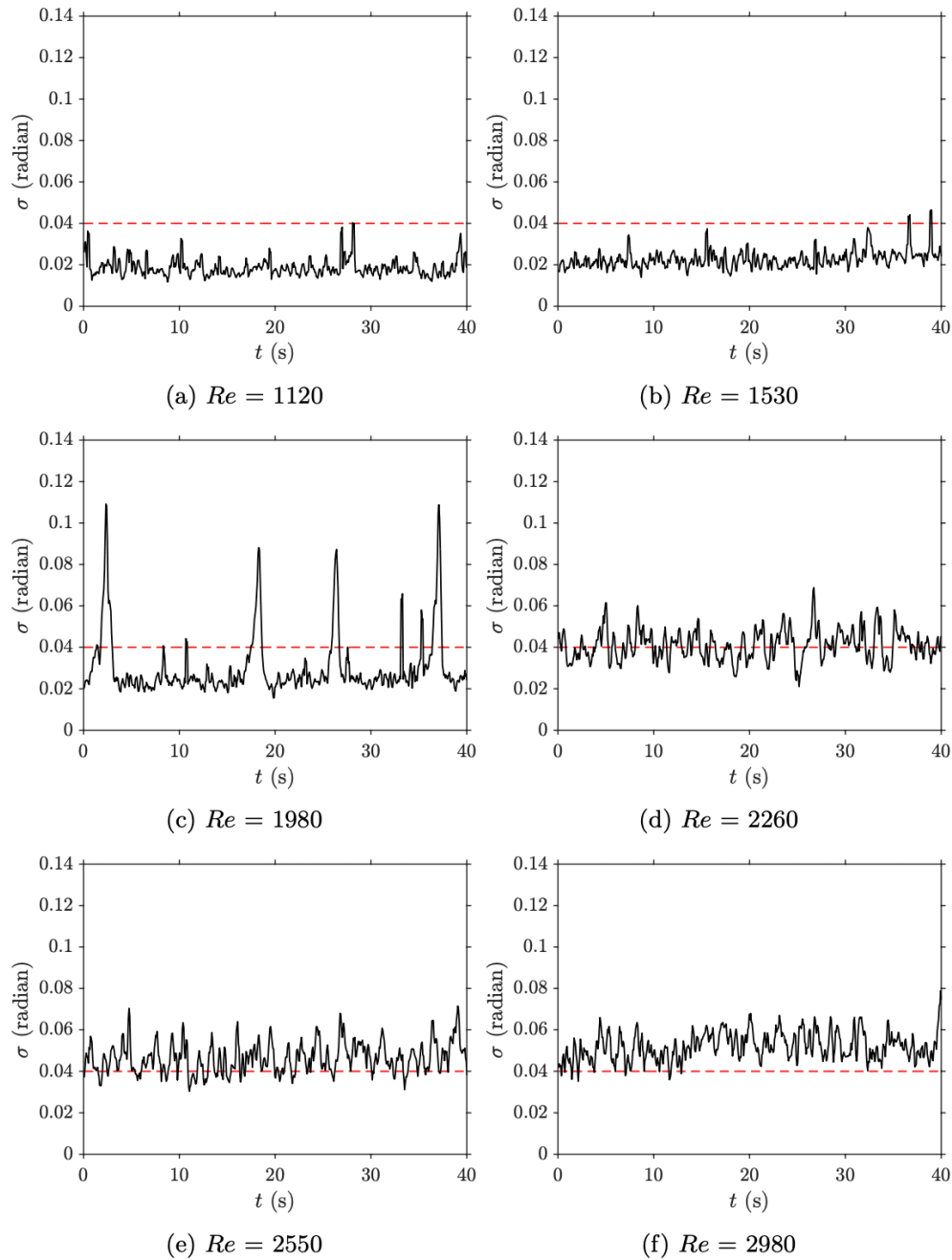


Figure 7. Variation of Standard Deviation over Time for different Reynolds Numbers for fluid-particle mixture ($\phi = 1.2 \times 10^{-3}$, particle size range = 212 – 250 μm): Subfigures depict the temporal evolution of standard deviation values calculated from streak angles obtained through frame analysis for six different Reynolds numbers. The x-axis represents time (in seconds), while the y-axis represents the standard deviation (in radians) of streak angles. Additionally, a red line at the standard deviation value of 0.04 serves as a reference for distinguishing between laminar, transient, and turbulent flow regimes.

We first conduct repeated measurements under conditions of relatively high and low Reynolds numbers ($Re = 1120$ and $Re = 7500$), representing fully turbulent and fully laminar flows respectively to assess lower and upper bounds for the values of standard deviation. By plotting standard deviation values while simultaneously validating them with the PIV setup, a reference red line ($\sigma = 0.04$) separating both cases is established (as depicted in Figure 7), serving as a benchmark for less obvious states between the fully turbulent and fully laminar reference cases. We also cross-check the nature of the flow for each value of Re presented in Figure 7 using the PIV system and the pressure drop system to further confirm the effectiveness of using the statistical distribution of streak angles in precisely understanding the flow characteristics.

The examination of subfigures in Figure 7 reveals more detailed information on the flow dynamics: For Figure 7(a) and (b), the flow is laminar (the standard deviation value throughout the time is well below the red line demarcation). As for the case within the transitional regime, found around $Re = 1980$, shown in Figure 7(c), clear peaks of standard deviation indicate intermittent turbulent patches (puffs) amidst predominantly laminar flow conditions: these are also observed through the PIV system. As the flow gradually transitions towards turbulence, exemplified by subfigure 7(d), the standard deviation progressively approaches and eventually surpasses the red line reference, indicating the onset of turbulent behavior. The turbulence invades a greater part of the signal and finally all of it in figures Figure 7(e) and Figure 7(f), where the standard deviation consistently exceeds the red line, signifying fully turbulent flow conditions.

The outcomes of the flow analysis conducted with the pressure drop setup (Figure 4) and the PIV system (table 3) closely match the conclusions given by the proposed visualization system. The analysis and comparison of each case to the reference plot shown in Figure 7 reinforce the identified trends in flow dynamics by the streak visualization method in not only identifying the nature of the flow but also detecting the presence of any transitional flow feature. Here, the identification of a simple threshold in the value of the standard deviation, calibrated from the purely laminar and purely turbulent state, makes it possible to reliably detect transient features such as puffs.

5.3. A new approach to the estimation of critical Reynolds number

The probability distribution of angles contains far more information on the flow than we have used so far. They contain a measure of how far the flow stands from the laminar or the fully developed turbulent state. Until now, we have only used a threshold on the standard deviation to detect whether any turbulence was present but without quantifying "how turbulent" the flow was. Doing this enables us to find a threshold where the flow becomes "closer" to the turbulent state than to the laminar state in the spirit of the approach

proposed by [15][62] to define a critical Reynolds number for the transition to turbulence. To quantify the idea of proximity between states, we propose utilizing the Kullback-Leibler (K-L) divergence. This statistical measure provides a means to quantify the difference between two probability distributions, offering a rigorous method for comparing observed angle distributions with reference distributions representing pure laminar and pure turbulent cases.

The KL divergence between two continuous distributions P and Q is given by:

$$D_{KL}(P \parallel Q) = \int_{-\infty}^{\infty} p(x) \log \left(\frac{p(x)}{q(x)} \right) dx. \quad (6)$$

Here $p(x)$ and $q(x)$ represent the probabilities of outcome x under distributions P and Q . By employing K-L divergence, we can effectively evaluate the degree of similarity or dissimilarity between a given angle distribution and the reference distributions [63]. This approach enables a robust assessment of flow conditions based on the observed angle data, facilitating the identification of laminar, turbulent, or intermediate regimes within the fluid.

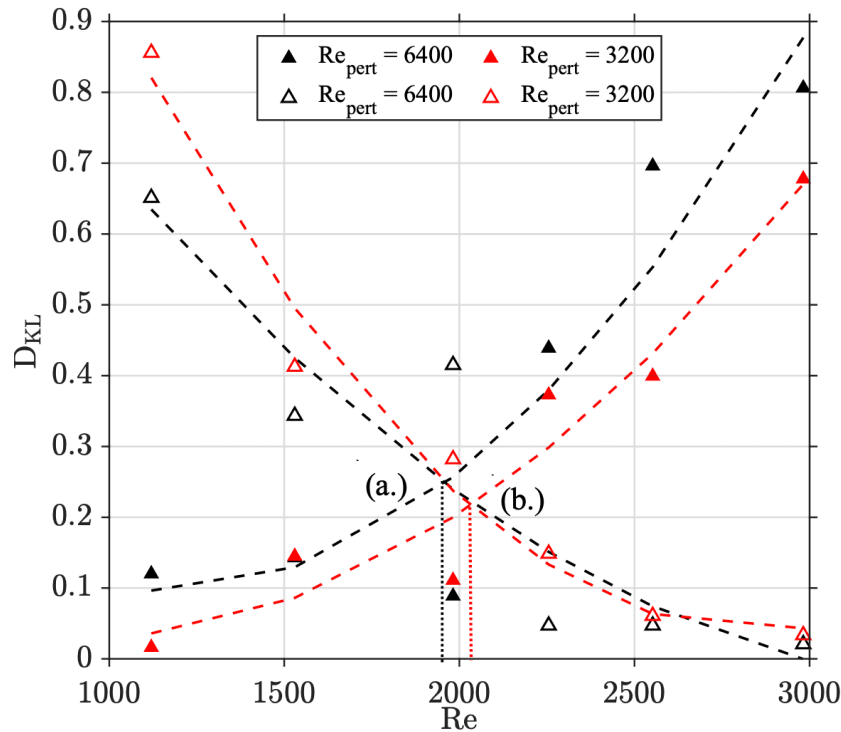


Figure 8. K-L divergence for the above-mentioned Re_{pert} having $\phi = 1.2 \times 10^{-3}$ and particle size range = 212 – 250 μm where working fluid is introduced as perturbation upstream of the setup. The solid markers in the illustration represent instances where a laminar flow streak angle probability distribution with $Re = 1120$ is taken as the reference case for calculating the K-L divergence in subsequent scenarios. Conversely, the hollow markers indicate situations where an Re of 4500 is adopted as the reference case.

As shown in Figure 8, for both the case of $Re_{\text{pert}} = 3200$ and $Re_{\text{pert}} = 6400$, the values of KL divergence ($D_{KL}(P|Q)$) increase with increasing Re when the reference probability distribution Q is taken from the laminar flow ($Re = 1120$). $D_{KL}(P|Q)$ takes higher values for higher Re as the presence of turbulence distorts the flow state away from the reference laminar state. At smaller Re , where flow is mostly laminar, the streak angle distribution is similar to that of the reference case at $Re = 1120$.

Conversely, the K-L divergence values decrease with increasing Re when the reference distribution Q is that of a turbulent case $Re = 4500$. Laminar states at low Re return a high K-L divergence, and those at higher Re remain close to 0, indicating a close match with the streak angle distribution of the $Re = 4500$, which is turbulent.

Hence, the K-L divergence provides a quantitative measure of the turbulent state based on the knowledge of particle angles of a reference case of either a pure laminar or pure turbulent flow scenario.

To estimate the critical Reynolds number Re_c using the graph (Figure 8), we sought a location where the K-L divergence exhibits a pronounced shift for both choices of laminar and turbulent reference distributions Q .

Specifically, the graph shows that for both the laminar ($Re = 1120$) and turbulent ($Re = 4500$) reference cases, there is a distinct crossover region where the divergence values change rapidly, right around the point of intersection of K-L values calculated with either reference for each case. For the case of $Re_{pert} = 3200$, this crossover occurs at a higher Re (see Figure 8 (b) in the graph), i.e., $Re > 2000$, suggesting that the transition to turbulence happens at a higher Reynolds number with smaller Re_{pert} . This is confirmed by the friction factor measurements shown in Figure 4, where the friction factor corresponds to that in the turbulent regime for $Re > 2000$. Conversely, for the higher perturbation case of $Re_{pert} = 6400$, the crossover occurs at a lower Re (see Figure 8 (a) in the graph), i.e., $Re < 2000$. This indicates that larger upstream perturbations induce an earlier transition to turbulence, which is also confirmed by the Figure 4 graph showing the friction factor in the transitional regime at these Reynolds numbers. This observation is consistent with the experimental findings showing the Friction factor vs Re graph by Ref. ^[30].

Hence, using the laminar and turbulent states as references offers a robust method to assess the point of transition to turbulence and the corresponding critical Reynolds number, using the K-L divergence.

6. Conclusion

The study demonstrates that the streak visualization technique reliably distinguishes between laminar, transitional, and turbulent flow regimes in particulate pipe flows through the quantification of streak angles, supported by validation from PIV and pressure drop measurements.

This finding underscores the potential for accessible and cost-effective methods to complement or replace traditional, resource-intensive techniques, broadening their field of application both in research and to practical applications in fluid dynamics

The results demonstrate that the streak visualization technique is an effective tool for distinguishing between flow regimes in particulate pipe flows. By analyzing streak angle distributions, the method reliably identifies laminar, transitional, and turbulent states. Validation through complementary methods, including Particle Image Velocimetry (PIV) and pressure drop analysis, further supports its accuracy. The use of statistical measures, such as the standard deviation of streak angles and the Kullback-Leibler divergence, enhances the ability to detect flow transitions and determine the critical Reynolds number,

effectively addressing the challenge of distinguishing erratic trajectories resulting from underlying turbulent fluid motion from regular trajectories associated to a laminar flow.

Some limitations remain, in particular the need for manual steps in image processing, which introduce subjectivity. However, automation of these steps and refinements to improve the system's robustness are not expected to pose a major challenge and could extend the application of this method to a wider range of scenarios. As such future developments of the method itself could focus on automated streak angle analysis and exploring applications in non-circular geometries or single-phase flows to expand the method's utility.

The findings align with existing literature on turbulence and transitional flow dynamics, in highlighting the role of particle behavior in influencing flow states. Compared to traditional methods like PIV and Laser Doppler Velocimetry (LDV), the streak visualization technique offers a more accessible and cost-effective alternative for the purpose of detecting laminar and turbulent flow patterns, without sacrificing reliability. This broadens its potential application in cases where resources for high-cost methods are unavailable.

However, the main scope to expand this method probably lies in the processing of the data it generates: while using a threshold on the standard deviation obtained by calibration against fully laminar and fully turbulent states offers a reliable, objective method to identify flow patterns, more advanced statistical analysis could be used to eliminate the calibration step. Indeed, despite its simplicity, streak velocimetry still collects extensive time-dependent flow data that was not used for the purpose of detecting flow patterns. The reliable definition of a transitional Reynolds number based on the KL divergence, certainly offers a glimpse of how more refined statistical analysis of the time-dependent statistical distribution of streak angles may provide deeper insight into the flow dynamics.

Acknowledgements

The authors would like to extend their gratitude to Ian Bates, lab technician at Coventry University, for his invaluable assistance. Special thanks to Lyse Brichet, intern (2022) and Mathilde Schneider, intern (2020–2021) from Ecole Normale Supérieure de Lyon, Université, for their assistance with data collection and ideation respectively. Additionally, the authors acknowledge the fluids research group of Fluids and Complex Systems at Coventry University for their support and collaboration.

References

1. [△]Breithaupt T, Ayers J. "Visualization and quantitative analysis of biological flow fields using suspended particles". In: *Zooplankton*. Routledge; 2021. p. 117–129.

2. [^]Pozniak S. *Business value from visualisation technologies*. Master's thesis, University of Stavanger, Norway (2017).
3. [^]Post FH, Vrolijk B, Hauser H, Laramée RS, Doleisch H. *Feature extraction and visualisation of flow fields*. In: *Eurographics (State of the Art Reports)*. 2002.
4. [^]Bujack R, Middel A (2020). "State of the art in flow visualization in the environmental sciences". *Environmental Earth Sciences*. 79 (2): 65.
5. [^]Zhou KC, Huang BK, Gamm UA, Bhandari V, Khokha MK, Choma MA (2016). "Particle streak velocimetry-optical coherence tomography: a novel method for multidimensional imaging of microscale fluid flows". *Biomed. Opt. Express*. 7 (4): 1590–1603. doi:10.1364/BOE.7.001590.
6. [^]Kumar S, Vasumathi M, et al. (2020). "Applying visualization techniques to study the fluid flow pattern and the particle distribution in the casting of metal matrix composites". *Journal of Manufacturing Processes*. 58: 668–676.
7. [^]Salwen H, Grosch CE (1972). "The stability of poiseuille flow in a pipe of circular cross-section". *Journal of Fluid Mechanics*. 54 (1): 93–112.
8. [^]Salwen H, Cotton FW, Grosch CE (1980). "Linear stability of poiseuille flow in a circular pipe". *Journal of Fluid Mechanics*. 98 (2): 273–284.
9. [^]Hof B, Juel A, Mullin T (2003). "Scaling of transition thresholds in pipe flows". *Physical Review Letters*. 91 (24): 244502.
10. [^]Manneville P (2015). "Turbulence in wall-bounded flows: A subcritical transition?" *European Journal of Mechanics-B/Fluids*. 49: 345–362.
11. [^]Wyganski IJ, Champagne F (1973). "On transition in a pipe. part 1. the origin of puffs and slugs and the flow in a turbulent slug". *Journal of Fluid Mechanics*. 59 (2): 281–335.
12. [^]Mullin T, Peixinho J (2006). "Recent observations of the transition to turbulence in a pipe". In: *IUTAM Symposium on Laminar-turbulent Transition*, pp. 45–55. Springer.
13. [^]Eckhardt B, Schneider TM, Hof B, Westerweel J (2007). "Turbulence transition in pipe flow". *Annu. Rev. Fluid Mech.* 39: 447–468.
14. [^]Barkley D (2016). "The rise of fully turbulent flow". *Journal of Fluid Mechanics*. 803: 1.
15. ^a, ^bAvila K, Moxey D, De Lozar A, Avila M, Barkley D, Hof B (2011). "The onset of turbulence in pipe flow". *Science*. 333 (6039): 192–196.
16. [^]Barkley D (2016). "Theoretical perspective on the route to turbulence in a pipe". *Journal of Fluid Mechanics*. 803: 1.

17. [^]Schmid PJ, Henningson DS, Jankowski D (2002). "Stability and transition in shear flows. applied mathematical sciences, vol. 142". *Appl. Mech. Rev.* 55 (3): 57–59.
18. [^]Pope SB (2001). "Turbulent flows". *Measurement Science and Technology*. 12 (11): 2020–2021.
19. [^]Matas J-P, Morris JF, Guazzelli E (2003). "Transition to turbulence in particulate pipe flow". *Physical Review Letters*. 90 (1): 014501.
20. [^][‡]Agarwal N, Choueiri GH, Hof B (2019). "Transition to turbulence in particle laden flows". *Physical Review Letters*. 122 (11): 114502.
21. [^]Segré G, Silberberg A (1962). "Behaviour of macroscopic rigid spheres in poiseuille flow part 2. experimental results and interpretation". *Journal of Fluid Mechanics*. 14(1): 136–157.
22. [^]Matas J-P, V. G, Morris JF, Guazzelli E (2004). "Trains of particle at finite reynolds number pipe flow." *Phys. Fluids*. 16(11): 4192–4195.
23. [^]Oliver R (1962). "Influence of particle rotation on radial migration in the poiseuille flow of suspensions". *Nature*. 194: 1269–1271.
24. [^]Repetti RV, Leonard EF (1964). "Segré–silberberg’s annulus formation: a possible explanation." *Nature*. 203: 1346–1348.
25. [^]Schonberg JA, Hinch EJ (1989). "Inertial migration of a sphere in poiseuille flow." *J. Fluid Mech.* 203: 517–524.
26. [^]Hogg AJ (1994). "The inertial migration of non–neutrally buoyant spherical particles in two–dimensional shear flows." *J. Fluid Mech.* 272: 285–318.
27. [^]Han M, Kim C, Kim M, Lee S (1999). "Particle migration in tube flow of suspensions." *J. Rheol.* 43: 1157–1174.
28. [^]Asmolov ES (1999). "The inertial lift on a spherical particle in a plane poiseuille flow at large channel reynolds number." *J. Fluid Mech.* 381: 63–87.
29. [^]Rouquier A, Pothérat A, Pringle CCT (2019). "An instability mechanism for particulate pipe flow". *Journal of Fluid Mechanics*. 870: 247–265.
30. [^][‡][‡]Hogendoorn W, Chandra B, Poelma C (2022). "Onset of turbulence in particle–laden pipe flows". *Physical Review Fluids*. 7 (4): 042301.
31. [^]Leskovec M, Lundell F, Innings F (2020). "Pipe flow with large particles and their impact on the transition to turbulence". *Physical Review Fluids*. 5 (11): 112301.
32. [^]Post FH, Van Walsum T (1991). "Fluid flow visualization". In: *Focus on Scientific Visualization*, pp. 1–40. Springer.
33. [^]Settles GS (1986). "Modern developments in flow visualization". *AIAA journal*. 24 (8): 1313–1323.

34. [^]Settles GS. *Schlieren and Shadowgraph Techniques: Visualizing Phenomena in Transparent Media*. Springer; 2001.
35. [^]Merzkirch W. *Flow Visualization*. Academic Press; 1987.
36. [^]Tropea C, Yarin AL, Foss JF, et al. *Springer Handbook of Experimental Fluid Mechanics*. vol. 1. Springer; 2007.
37. [^]Comte-Bellot G (1976). "Hot-wire anemometry in fluid mechanics research". *Annual Review of Fluid Mechanics*. 8: 209–231.
38. [^]Bradshaw P. *An Introduction to Turbulence and Its Measurement*. Pergamon Press; 1971.
39. [^]Ferrari S, Rossi R, Di Bernardino A (2022). "A review of laboratory and numerical techniques to simulate turbulent flows". *Energies*. 15 (20): 7580.
40. [^]Adrian RJ (1991). "Particle-imaging techniques for experimental fluid mechanics". *Annual Review of Fluid Mechanics*. 23 (1): 261–304.
41. [^]Adrian RJ (2005). "Twenty years of particle image velocimetry". *Experiments in fluids*. 39: 159–169.
42. [^]Raffel M, Willert CE, Scarano F, Kähler CJ, Wereley ST, Kompenhans J. *Particle Image Velocimetry: a Practical Guide*. Springer; 2018.
43. [^]George WK, Lumley JL (1973). "The laser-doppler velocimeter and its application to the measurement of turbulence". *Journal of Fluid Mechanics*. 60 (2): 321–362.
44. [^]Albrecht H-E, Damaschke N, Borys M, Tropea C. *Laser Doppler and Phase Doppler Measurement Techniques*. Springer; 2013.
45. [^]Adrian RJ (2017). "Laser velocimetry". In: *Fluid Mechanics Measurements*, pp. 175–299. Routledge.
46. [^]Coupland JM (2000). "Laser doppler and pulsed laser velocimetry in fluid mechanics". In: *Photomechanics*, p. 373–412. Springer.
47. [^]Schultz A, Cruse H, Zare R (1972). "Laser-induced fluorescence: A method to measure the internal state distribution of reaction products". *The Journal of Chemical Physics*. 57(3): 1354–1355.
48. [^]Crimaldi JP (2008). "Planar laser induced fluorescence in aqueous flows". *Experiments in Fluids*. 44: 851–863.
49. [^]Dash A, Hogendoorn W, Oldenziel G, Poelma C (2022). "Ultrasound imaging velocimetry in particle-laden flows: counteracting attenuation with correlation averaging". *Experiments in Fluids*. 63(3): 56.
50. [^]Poelma C (2017). "Ultrasound imaging velocimetry: a review". *Experiments in Fluids*. 58: 1–28.
51. [^]Elkins CJ, Alley MT (2007). "Magnetic resonance velocimetry: applications of magnetic resonance imaging in the measurement of fluid motion". *Experiments in Fluids*. 43 (6): 823–858.
52. [^]Hartung MP, Grist TM, Francois CJ (2011). "Magnetic resonance angiography: current status and future directions". *Journal of Cardiovascular Magnetic Resonance*. 13 (1): 19.

53. ^a Singh S, Pothérat A, Pringle CC, Bates IR, Holdsworth M (2020). "Simultaneous eulerian--lagrangian velocity measurements of particulate pipe flow in transitional regime". *Review of Scientific Instruments*. 91 (9).
54. ^Δ Durst F, Ray S, U{nsal B, Bayoumi O (2005). "The development lengths of laminar pipe and channel flows".
55. ^Δ OpenCV-Python: Open Source Computer Vision Library in Python. <https://github.com/opencv/opencv-python>.
56. ^Δ Hough PV. Method and means for recognizing complex patterns. Google Patents. US Patent 3,069,654 (1962).
57. ^Δ Duda RO, Hart PE (1972). "Use of the hough transformation to detect lines and curves in pictures". *Communications of the ACM*. 15 (1): 11–15.
58. ^Δ Canny J (1986). "A computational approach to edge detection". *IEEE Transactions on Pattern Analysis and Machine Intelligence*. (6): 679–698.
59. ^Δ Matas J, Galambos C, Kittler J (2000). "Robust detection of lines using the progressive probabilistic hough transform". *Computer Vision and Image Understanding*. 78 (1): 119–137.
60. ^Δ Hogendoorn W, Poelma C (2018). "Particle-laden pipe flows at high volume fractions show transition without puffs". *Physical Review Letters*. 121 (19): 194501.
61. ^Δ Joseph DD, Yang BH (2008). "Friction factor correlations for smooth pipes". *Journal of Fluid Mechanics*. 123: 456–478.
62. ^Δ Mukund V, Hof B (2018). "The critical point of the transition to turbulence in pipe flow". *Journal of Fluid Mechanics*. 839: 76–94.
63. ^Δ Basseville M (2013). "Divergence measures for statistical data processing—an annotated bibliography". *Signal Processing*. 93 (4): 621–633.

Declarations

Funding: No specific funding was received for this work.

Potential competing interests: No potential competing interests to declare.